Nanometric metrology by FIB-SEM-DIC measurements of strain field and fracture separation on composite metallic material

Y. Mammadi, A. Joseph, A. Joulain, J. Bonneville, C. Tromas, S. Hedan, V. Valle

Version of Record: https://www.sciencedirect.com/science/article/pii/S0264127520301994
Manuscript_557dfc4766aa5615def29599f8809f92

Nanometric metrology by FIB-SEM-DIC measurements of strain field and fracture separation on composite metallic material

Y. MAMMADI[a], A. JOSEPH[a], A. JOULAIN[a], J. BONNEVILLE[a], C. TROMAS[a], S. HEDAN[b] and V. VALLE[a]

[a]*Institut PPRIME, University of Poitiers, CNRS, ENSMA, UPR 3346, 8696, Chasseneuil Cedex, France*
[b]*Institut IC2MP, University of Poitiers, CNRS, UMR 7285, ENSI Poitiers, 86073 Poitiers cedex9, France*

ARTICLE INFO

Keywords:
Fracture
FIB-SEM-DIC
Image correlation
Residual strains

ABSTRACT

Currently, kinematic field measurements for studying the mechanical behavior of materials and structures use common optical methods, such as mark tracking techniques, grid methods and correlation techniques. These techniques are employed over a region of interest ranging from micro to millimeter scale. However, when studies need to be conducted on even smaller scales such as sub-micrometric scale, the use of more complex means of observation is required. In this case, the work can be achieved using the scanning electron microscope (SEM), and the Focused-Ion-Beam (FIB) as marking technique. An adaptation of Digital Image Correlation (DIC) method Heaviside-based Digital Image Correlation (H-DIC) is chosen to investigate the mechanical behavior and taking into account local fractures. As the studied problem is to extract strains from a fractured material using a displacement field measurement method, derivative computation for strain determination is not well adapted. The proposed approach consists in extracting the residual strains from local first gradients of H-DIC, which are less perturbed by the fractures. Various tests were performed to evaluate the validity of this new proposed approach. An application to study the mechanical behavior of a metallic composite (Al/ω-Al-Cu-Fe) is proposed. A particular exploitation of all field lies in the good separation of the strain fields and the cracked part. A discussion that focus on the comparison between a conventional DIC analysis and its extension was presented on the zones without or with fractures.

1. Introduction

Scanning Electron Microscopy (SEM) is a powerful tool to observe material behavior and deformation at a small scale by an analysis of numeric images. Recently, these observations have been extended to access to the quantitative mechanical characterizations with a nanometric spatial resolution [21–23]. To estimate certain properties in fundamental mechanics, it is necessary to measure displacements and deformations at the micron and sub-micron scales. The Digital Image Correlation (DIC) [7, 29, 30], which was developed in the 1980s is one of the methods applicable to micro/nanometric measurements. [15, 25]. The DIC method is an optical technique that is widely used in mechanics because of its ability to determine displacement fields, to access to deformation fields [20, 37], and to detect cracks, for material property identification procedures. Moreover, it is easy to implement and has a high accuracy. This robust method has emerged for the experimental quantification of 2D deformation fields in microstructural-scale planes [4, 28, 33]. DIC method has been carried out [32] and called SEM-DIC.

The combination of these powerful techniques SEM and DIC has been used in a wide range of materials to study nanoscale and microscopic phenomena [12, 13, 31]. However, experimental data using SEM-DIC and issued from mechanical localization (fracture, sliding bands, ...) remain limited. With SEM-DIC, the first difficulty is to have sufficient speckle contrast in the SEM images. However, the accuracy of the measurements is directly linked to the contrast given by the material arrangement. Most of the materials give uniform contrast under SEM imaging. For these materials, some techniques have been developed to retrieve a good contrast. One of them is to chemically etch the observed surface. These techniques offer the possibility to mark the whole surface of the specimen in one process, but some chemical modifications of the material can occur. A second way is to deposit particles of another material [24, 26, 37]. This process enables to cover the total surface of the specimen, but the added material can diffuse into the specimen.

younes.mammadi@univ-poitiers.fr (Y. MAMMADI); valery.valle@univ-poitiers.fr (V. VALLE)
ORCID(s): 0000-0001-5597-6180 (Y. MAMMADI)

The more recent techniques use the ablation principle using Focused Ion Beam (FIB). Two methods were considered, the first one consists of depositing a layer of platinum and then milling it using FIB [37]. The second method consists in milling directly the specimen surface of the specimen using FIB [15]. Using these two last techniques makes marking the total surface of the specimen more difficult, but the process is easier for small surfaces. It can be noticed that even for small milling depth (a few tens of nanometers), local damages have been observed in the literature [16] generating local residual strains [27, 36] on the specimen surface. In the present work, these induced residual strains are neglected for two main reasons. Firstly, contrarily to the previous studies, our specimen has large dimensions and the damaged depth is therefore extremely small comparatively to the specimen thickness. Secondly, all loading steps are compared to the initial step where the damaged surface is already present.

The major difficulty is linked to the SEM and the problem of image stability and distortion [31]. In contrast to the proven performance of the DIC methods using optical images, SEM-DIC suffers of lakes directly associated with instability and distortion of the SEM tools. This issue of image drift has been analyzed in previous studies [17, 28] and, leading to these recommendations, the local measurement displacement error can be evaluated to nearly 0.05 pixel[18].

The last difficulty, linked to the material behavior to be analyzed, is to correctly observe and separate strain localization and fracture developments. Using conventional DIC in optical condition, some works have been done on materials with developed cracks [32] but it is always difficult to localize cracks and to measure accurately strain fields. As the conventional DIC was developed on continuum mechanics basis, this method is clearly not adapted to the observation of cracked materials. Recently, a global approach gave interesting results [3], but this method supposed the knowledge of the crack position before image analysis. A more recent work propose a local approach [2, 9], adding a specific enrichment of the kinematical field transformation, taking into account the presence of cracks [33–35]. This method, the Heaviside-based digital image correlation (H-DIC), has the advantage to analyze images without knowing the crack positions, orientations and magnitudes of aperture and shear. As the proposed enrichment of this method is the sum of a classical first displacement gradient tensor (representing local strains) and a jump vector (representing the local kinematic behavior of crack), it can be possible to measure discontinuous displacement fields. However, actually, the strain tensor is computed from the displacement field (which should be continuous), using finite differences (FD) [1]. This process does not guarantee the good separation of the strain from the displacement field which can amplify in presence of crack. The most important problem is that the strains, evaluated using discontinuous displacement give over-evaluated wrong values. The aim of the proposed paper is to :

- Describe an optimized procedure of separation of the strain part and the crack part.
- Define the process of marking and analysis using FIB and SEM equipment.
- Evaluate the performances of the SEM-DIC tool.
- Investigate these developments to the study of a metallic composite material.

2. Methods and materials

2.1. Separation of strains and cracks using a Heaviside-based digital image correlation method

Heaviside-based digital image correlation method [33] is an adapted technique based on local DIC approach to be able to extract cracks using an enrichment of the kinematical transformation used in DIC process Eq. 1. This method was used to capture cracks without knowing their position and orientation and it was applied to different materials and in different domains [6, 8]. This method was also extended in stereo to capture cracks with out-of-plane displacements (H-SDIC)[34], and in 3D using μCT equipment for the study of cracks inside materials (H-DVC) [34]. The kinematical transformation can be expressed as :

$$\underline{X}^* = \underbrace{\underline{X} + \overbrace{\underline{U}}^{\text{Rigid body}} + \overbrace{\frac{\partial \underline{U}}{\partial \underline{X}}\left(\underline{X} - \underline{X}_0\right)}^{\text{First gradient}}}_{\text{Conventional DIC method}} + \underbrace{\overbrace{\underline{U'}}^{\text{Jump vector}} \times \overbrace{H\left(\underline{X} - \underline{X}_0\right)}^{\text{Heaviside function}}}_{\text{Heaviside-DIC method}} \tag{1}$$

where $\underline{X}$ is the position of the subset in the reference image, $\left(\underline{X} - \underline{X}_0\right)$ is the position in the subset and $\underline{U}$ is a translation in the plane. The jump/step function defines the magnitude of the kinematic discontinuity in both the

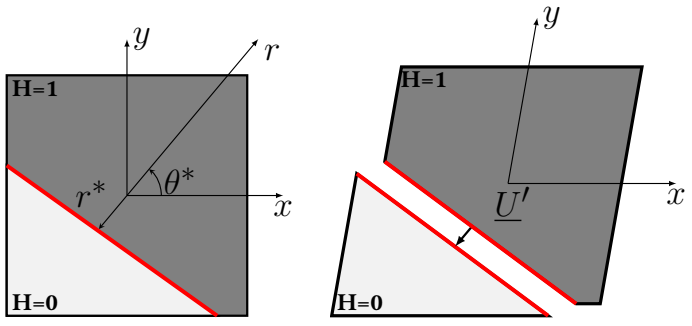

(a) Reference subset (b) Subset after deformation

Figure 1: Subset representation of the effect of Heaviside function from the initial (a) to the final (b) state. The kinematical transformation is composed by a rigid body movement (not represented here) a displacement jump $\underline{U}'$ and a deformation.

horizontal and the vertical directions represented by the jump vector $\underline{U}'$ in Fig. 1. Using polar coordinates of the discontinuity (r^*, θ^*), the Heaviside function describes the precise discontinuity at any orientation θ^* as well as the distance r^* from the center of the subset:

$$H\left(\underline{X}-\underline{X_0}\right)=H\left(x,y,r^*,\theta^*\right)=H\left(x\cos\left(\theta^*\right)+y\sin\left(\theta^*\right)-r^*\right) \tag{2}$$

where (x,y) are the coordinates of a point in the subset.

Fig. 1 illustrates the location of the kinematic discontinuity.

The Heaviside function thus describes this discontinuity and allows the displacement of one side of the subset with respect to the other with a magnitude equal to the jump vector $\underline{U}'$. Schematically, the process can be represented as in Fig. 1, where the use of the Heaviside function authorizes the subset to be cut into two parts, and where each part corresponds to a particular kinematical transformation $\varphi_1\left(\underline{X}\right)$ and $\varphi_2\left(\underline{X}\right)$:

$$\begin{aligned}\varphi_1\left(\underline{X}\right)&=\underline{X}+\underline{U_1}+\frac{\partial U}{\partial X}\left(\underline{X}-\underline{X_0}\right)\\ \varphi_2\left(\underline{X}\right)&=\underline{X}+\underline{U_2}+\frac{\partial U}{\partial X}\left(\underline{X}-\underline{X_0}\right)\end{aligned} \tag{3}$$

- On domain H=0 depending on r^*,θ^*

$$\varphi_1\left(\underline{X}\right)=\underline{X}+\underline{U_1}+\frac{\partial U}{\partial X}\left(\underline{X}-\underline{X_0}\right) \tag{4}$$

- On domain H=1 depending on r^*,θ^*

$$\varphi_2\left(\underline{X}\right)=\underline{X}+\underline{U_2}+\frac{\partial U}{\partial X}\left(\underline{X}-\underline{X_0}\right) \tag{5}$$

Finally, the optimized solution S was computed using a Newton Raphson algorithm where all parameters were computed at the same time, and for each subset (i.e. local approach). It can be written as:

$$S\left(u,v,\frac{\partial u}{\partial x},\frac{\partial v}{\partial x},\frac{\partial u}{\partial y},\frac{\partial v}{\partial y},u',v',\theta^*,r^*\right) \tag{6}$$

with u',v' the components of the jump vector, $\frac{\partial u}{\partial x}$,$\frac{\partial v}{\partial x}$,$\frac{\partial u}{\partial y}$,$\frac{\partial v}{\partial y}$ the first gradient tensor.

The jump vector $\underline{U}'$ calculated during the optimization process has been extracted to analyze sliding movement at crystal scale [6], without using a post-processing algorithm based on the displacement maps. This approach has the

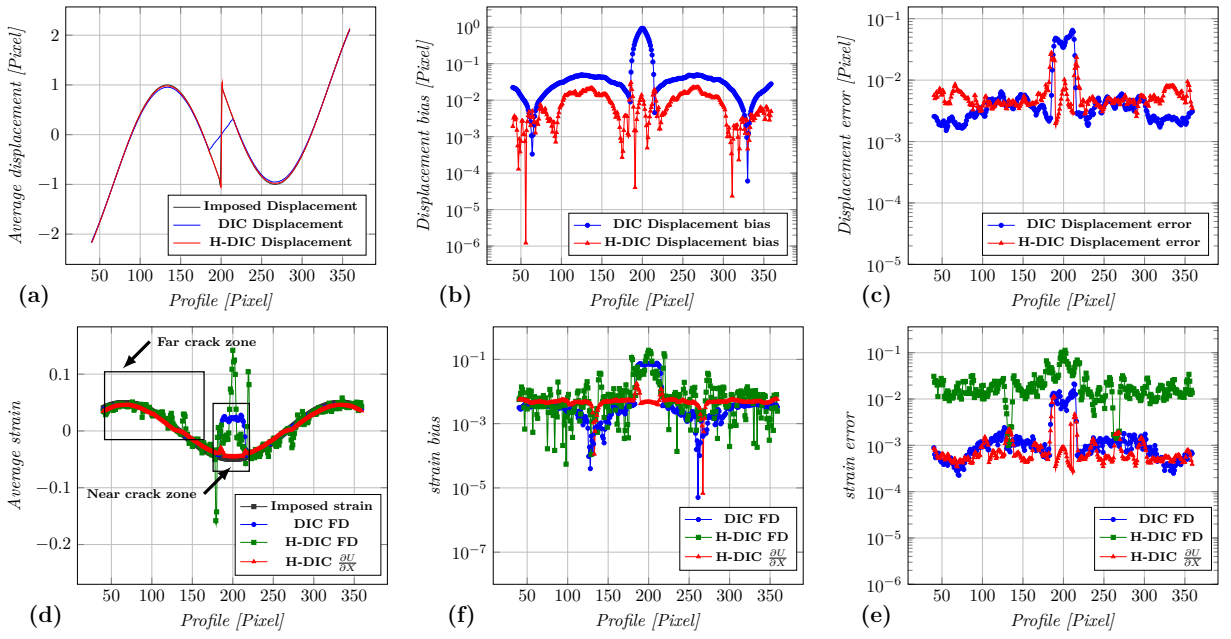

Figure 2: Comparison between conventional (DIC) and (HDIC), using internal $\frac{\partial U}{\partial X}$ and derivated parameters. (a) Average imposed and measured displacement, (b) calculated displacement bias, (c) calculated displacement standard deviation and finite difference (FD) (d) Average imposed and measured strain (see Table 1), (e) strain bias, (f) strain standard deviation. Rectangles correspond to calculation zone, near and far the crack.

Table 1
Comparison between different Tresca strain mean values computed from loading machine : Overall average and Local average Internal H-DIC error and bias and External H-DIC error and bias.

Mean Internal External Strain %								
	Displacement error (pixel)		Strain error %			Strain bias %		
	DIC	H-DIC	DIC FD	H-DIC FD	H-DIC $\frac{\partial U}{\partial X}$	DIC FD	H-DIC FD	H-DIC bias $\frac{\partial U}{\partial X}$
Zone without crack	0.003	0.004	0.089	1.812	0.072	0.262	0.780	0.466
Zone including one crack	0.04	0.004	0.908	6.340	0.064	7.092	9.280	0.457

advantages of giving the local value of the jump and no other hypothesis was added to extract the searched parameter $\underline{U}'$ using post-processing of the displacement field.

Actually, the employment of FD method from a discontinuous displacement field $\underline{U}$ (obtained from H-DIC) gives wrong strains at the vicinity of the crack path and high noisy data far from it (Fig. 1 (a)). This fact is due to the basis of the finite difference method which is only valid on continuum functions [1]. To solve problem it is proposed, using an identical approach than those previously employed for the jump vector $\underline{U}'$ evaluation, to extract the local gradient tensor $\frac{\partial U}{\partial X}$ calculated during the optimization process [6] (Fig. 1 (b)).

To compare the post-processing approach using FD method and the local strain approach using the first gradient without post-processing step, a pseudo strain indicator ε_{eq} was calculated in the spirit of Tresca :

$$\varepsilon_{eq} = \frac{|\varepsilon_1 - \varepsilon_2|}{2} \tag{7}$$

where ε_1 and ε_2 are the principal strains calculated from the displacement field using finite differences (FD) between neighborhood subsets or directly using local first gradients $\frac{\partial U}{\partial X}$.

Displacement and strain results are compared using synthetic images mimicking a sinusoidal evolution of the

(a) Dual-beam microscope

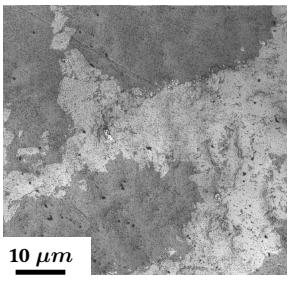

(b) Zone Z1 before patterns

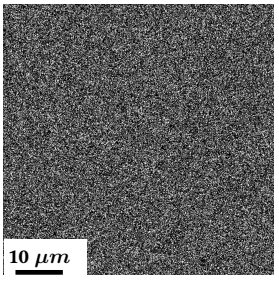

(c) Speckled patterns

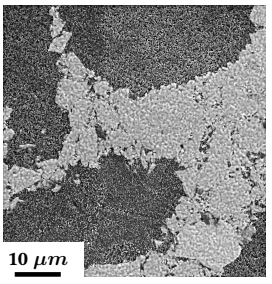

(d) Zone Z1 Speckled patterns

Figure 3: (a) FIB Dual-Beam microscope (b) Zone Z1 before FIB patterning , (c) Speckle pattern bitmap image (d) Zone Z1 after FIB patterning

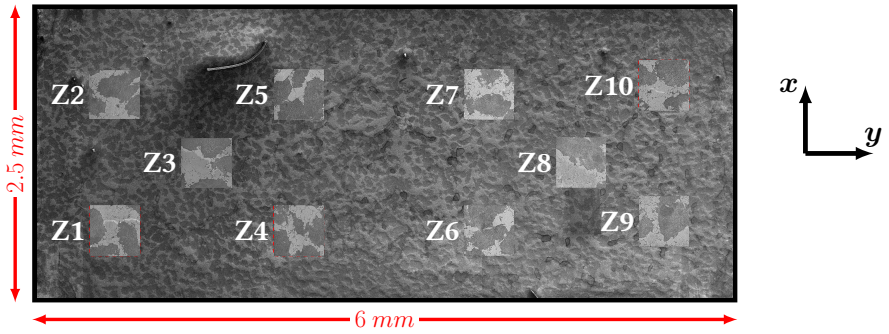

Figure 4: SEM image of the specimen, and zoomed parts of each analysed zone, Zone Z1, Z2... and Z10

.

strains superimposed to a crack (discontinuous displacement). DIC computation processes are performed using equal size subsets of 48×48 pixels, and repeated every pixels (grid step equal to 1 pixel). Results are obtained by averaging data along the crack axis. In Fig. 2, profiles were extracted to better see the behavior of different analyses. Fig. 2 (a) shows the excellent result of the imposed displacement using the H-DIC compared to conventional DIC. Fig. 2 (b) and (c) show bias error (systematic error) and standard deviation (arbitrary error) on the calculated displacement for the two algorithms. It can be retrieved the earlier results [33] showing an equivalent response of the two algorithms far from the crack and an excellent capture of the crack by H-DIC method contrarily to DIC. Fig. 2 (d), (e), (f) present the plots of the average strain, strain bias and strain error, respectively. These figures show that the use of the FD method to extract the local strains is a good process for conventional DIC outside of the vicinity of the fractured zone (zone called âĂIJfar the crack tipâĂİ on Fig. 2 (d)). However far and in crack zones, the use of a FD method on H-DIC displacement maps is not an appropriate choice. Indeed, as H-DIC method produces high-frequency displacement errors contrarily to conventional DIC, which can be assimilated as a low pass filter, the FD method gives high noises on strain maps (Fig. 2 (f)). Regardless of the presence of a crack in the subset, the better solution for strain extraction is to use the first gradients $\frac{\partial U}{\partial X}$ of Eq. 1 (Table 1). Table 1 confirms that the displacement errors are very low when the area does not contain any crack (0.003 pixel for DIC and 0.004 pixel for H-DIC). Without crack in the zone and in contrast to FD approach of H-DIC, the results of Table 1 confirms that FD approach of DIC [1] and first gradients $\frac{\partial U}{\partial X}$ of H-DIC can be used to measure the strains. In presence of one crack, the displacement errors remain unchanged for H-DIC (0.004 pixel) but increase of one order of magnitude with a value close to 0.03 pixel for the DIC. The best choice to study the strains in presence or not of cracks is the use of the first gradients $\frac{\partial U}{\partial X}$ of H-DIC algorithm because the strain errors and the strain bias were in the ranges of 0.064 to 0.072% and 0.457 to 0.466%, respectively. The errors and the bias measured from the FD approaches (DIC and H-DIC) were significantly greater (Table 1) with the values between one to two orders of magnitude higher than the first gradients $\frac{\partial U}{\partial X}$ of H-DIC algorithm.

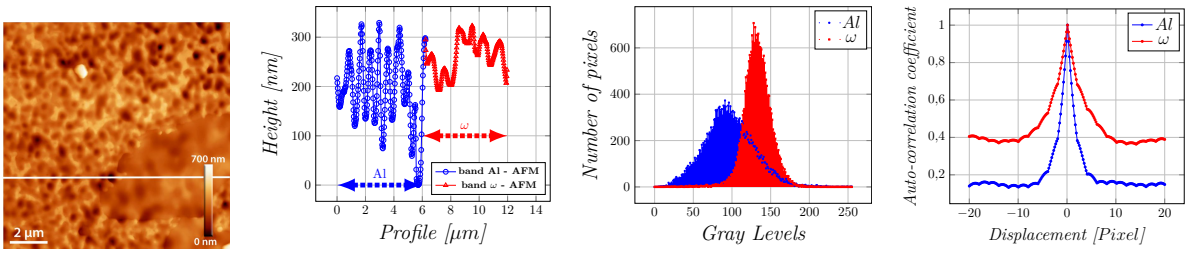

(a) (b) (c) (d)

Figure 5: Speckle quality evaluation. (a) AFM Image of a zone including the two phases. (b) Height profile from the corresponding white line. (c) Histograms of phases Al and ω. (d) Auto-Correlation of phases Al and ω.

2.2. Marking process

SEM-DIC requires the presence of a random pattern on the surface of the material. This pattern must have a recognizable and a resolvable structure at an appropriate scale serving the problem of interest. Random pattern marking remains a big challenge because of the small size studied and the very low amplitudes of mechanical phenomena (cracks and strains). Scrivens et al. [10] developed chemical vapor exposure and UV lithography with active random models for nanoscale and micro-scale measurements ($1 - 10\mu m^2$). Berfield et al. [2] randomly created speckle models with a fine-point airbrush for micro-scale ($100\mu m^2$) measurement and fluorescent nanoparticles for nanoscale measurements ($10\mu m^2$) [15]. On the other hand, ion-beam assisted deposition is a process in which the precursor gas is allowed to chemisorption on the sample surface, so that it will be broken down into volatile and non-volatile components by the bombardment of an incident energetic ion-beam ($10^4\mu m^2$). The non-volatile component, such as platinum (Pt), remains on the surface as a deposit. The reaction occurs only at positions where the ion-beam passes through the holes of a prepared mask model causing a designed speckle pattern [37]. Another way to create a SEM contrast is to use the FIB method by milling ($10^4\mu m^2$). The marking process of optimal speckle models by ion milling has been studied by Li et al. [15]. In the same way, our microstructure was built with a FIB system using an input pattern image (Fig. 3 (c)). Characteristics of this image can be controlled by the user and allow us to build a random speckle pattern on the investigated surface Fig. 3 (d). In our study, this dual-beam microscope (FIB-SEM, Helios NanoLab G3 CX) (Fig. 3 (a)) was used because it is easy to implement and image characteristics can be adapted to our material at our scale of measurement. This milling technique is repeated 10 times on the specimen surface (Fig. 4). The SEM image obtained from the natural aspect of the specimen (Fig. 3 (b)), where the two phases (ω and Al) of the composite material can be observed. Fig. 3 (c) shows the synthetic speckle pattern used for the milling of the specimen. Fig. 3 (d) presents the corresponding milled surface of the specimen. It can be observed that the specimen surface exhibits different aspects linked to the different phases of the composite material. Using FIB milling to create speckle patterns not only extends the application of FIB but also offers an efficient patterning technique for DIC method. In our experiments, FIB Helios field FIB-SEM (Fig. 3) is employed with the following milling parameters : acceleration voltage of $30keV$, beam current of $2.5nA$, working distance (WD) of 4mm and Horizontal Field Width (HFW) of $160\mu m$.

2.3. Imaging acquisition process

The principal difference between a conventional SEM imaging and a SEM quantitative imaging for metrology, is to respect the same principle applied using an optical system. As the acquisition of the SEM maps was done before loading and after unloading, parameters of the SEM microspope should not be modified during the entire test. The SEM parameters were selected according to the references of Kammers and Daly [13] ($20keV$, WD = $16mm$, HFW> 100 μm), Stinville et al. [28] ($5keV$, WD = $5mm$, HFW = $85\mu m$) and Mello et al [19] ($5keV$, 5 <WD< $10mm$, HFW = $60\mu m$), to minimize the distortion errors associated with SEM imaging. According to these works, acceleration voltages ($15keV$) and HFW ($160\mu m$) have been used to minimize the charging effects and further reduce drift distortion. In order to achieve higher spatial imaging resolution and electron beam stability, working distance was chosen equal to $10mm$. Thanks to these parameters, the elimination of SEM beam defects associated with a scanning generator microscope is optimized [18] .It has been possible to measure displacements with an accuracy better than 0.05 pixel, corresponding to $6.25nm$ (magnification $\gamma = 125nm/pixel$). To better investigate the metrological performances of our tools, it is necessary to continue the analysis on the chosen material. This one is briefly presented below.

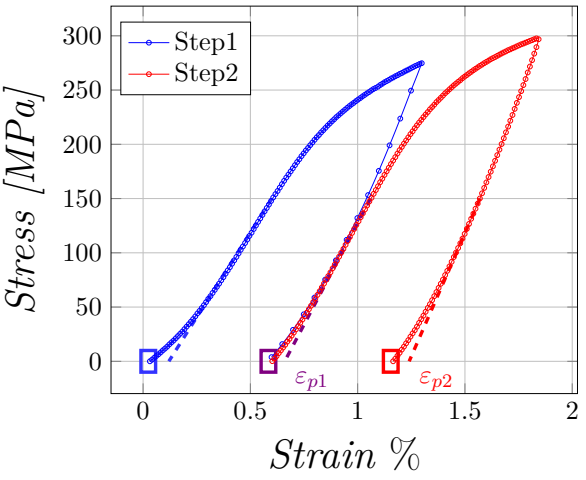

Figure 6: Stress strain plots given by the loading machine, for Step 1 (blue) and Step 2 (red). The rectangles correspond to captured images for DIC evaluation. ε_{p1}, ε_{p2} relate to plastic compression strain evolution of the specimen

2.4. Material description

Al/ω-Al-Cu-Fe composites combine a ductile Al matrix with brittle Al-Cu-Fe intermetallic reinforcement. Because ω-Al-Cu-Fe particles are hard particles, plastic deformation of the Al/ω-Al-Cu-Fe composite takes place in the Al matrix only [11, 14]. However, due to the high-volume fraction of ω-Al-Cu-Fe particles (40%), the latter percolate to form a hard skeleton that must be first fractured to allow plastic deformation in the Al matrix [14]. This also yields to very localized plastic deformation. Therefore, these composite materials are particularly well suited for testing a DIC method adapted to local plastic deformation and fracture. Small cylinders ($\phi = 8$ mm, h = 8 mm) of Al/40 vol% ω-Al-Cu-Fe composites were produced by the Spark Plasma Sintering (SPS) powder metallurgy technique. They were reactively sintered at T=823 K under a uniaxial pressure P = 100 MPa for 2 min. All details regarding powder processing and SPS parameters can be found elsewhere [11].

2.5. Evaluation of the speckle characteristics

To choose speckle characteristics and to evaluate the performances of our experimental approach, three parameters have been used to drive our choice. The first was an evaluation of the milling depth by Atomic Force Microscopy (AFM) measurement (Fig. 5 (b)) corresponding to a profile of depth (see the white straight line of Fig. 5 (a)). The second is the resulting image histograms and covariograms (Fig. 5 (c) and (d)), and the third, is a rigid body movement test and the error evolution during the time. For the ω phase of the material, the maximum depth reached 120 nm and the minimum depth is 30 nm. The Al phase is more milled with a maximum depth of 300 nm and a minimum depth of 200 nm. The speckle is less marked on the ω phase because its sputtering rate is lower than that of the Al phase. (Fig. 5). The graylevel histograms shows a more marked contrast on the ω phase (Fig. 5 (c)). It shows that on the Al phase a significant contrast with a maximum value close to 180 can be seen, in comparison with the ω phase where the contrast is less marked with a value of close to 90. The auto-correlation curve shows that the correlation technique is less efficient on the ω phase than on the Al phase (Fig. 5 (d)), introducing more calculation errors. It can be concluded that the measurement error should be greater on the ω phase.

2.6. Sample preparation, mechanical testing and microscopy

A compression sample, with a cross section of 2.5mm×2.5mm and a length of 6mm, was extracted from a SPS cylinder using a wire saw. It was mechanically polished using successive higher grades of SiC abrasive sheets and further polished for a good quality surface with diamond sprays up to a mirror surface aspect. Then, artificial random speckle zones were designed on the polished surface using FIB milling. Ten zones were thus created and chosen to be distributed over the sample surface. Each zone was captured 3 times by SEM imaging before the first loading/unloading cycle, after the first loading/unloading cycle (ε_{p1}) and after the second loading/unloading cycle (ε_{p2}), (see dotted lines in Fig. 6). Note that, for the sake of clarity, the nonlinear "toe-in" portion of the stress strain curves, resulting from small

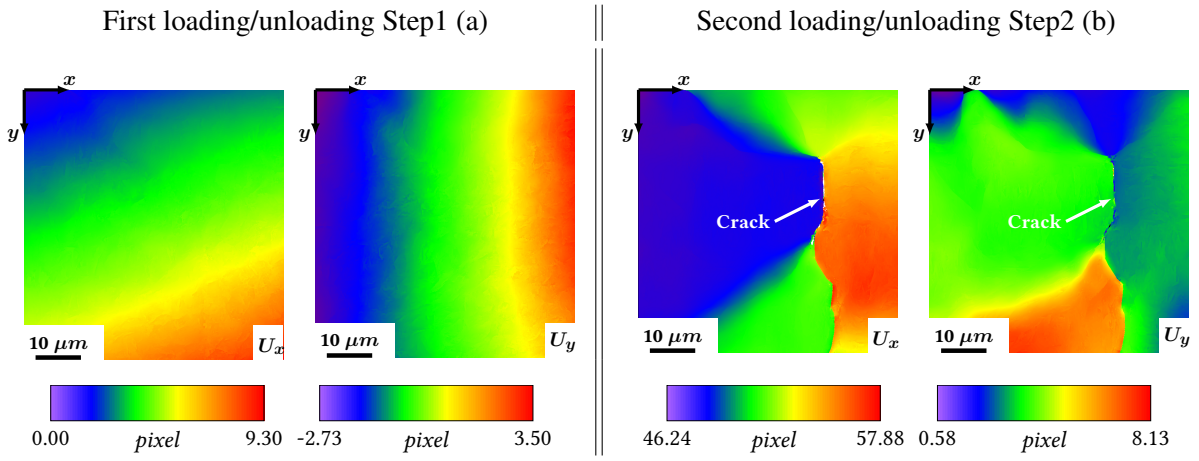

Figure 7: Ux and Uy measured displacement components from H-DIC computation for zone Z1 and first loading/unloading cycle Step1 (a), and for second loading/unloading cycle Step2 (b)

misalignment of the loading device, have been linearly fitted with the straight portion of the elastic stage. From the stress-strain curves reported in Fig. 6, it can be estimated that the SEM imaging of the speckle zones were performed at strains ε_p of 0% and at approximately 0.67% and 1.23% (Fig. 6). The sample was deformed at room temperature and a nominal constant strain rate of $\dot{\epsilon} = 1.4 \times 10^{-4}\ \ s^{-1}$. Compression tests were performed on an Instron 1195 type testing machine using an inverted compression device similar to the one described in [5].

After each loading-unloading cycle (i.e. step 1 and step 2), the sample is replaced at the same initial position in the SEM, and each zone is recovered. As it is difficult to retrieve the exact positions and orientations, the presented displacement maps are not representative of the actual movements of each zone during the mechanical test. However jump maps and strain maps do not need the exact positions and orientations to give genuine data. To show the ability to capture unperturbed maps, with discontinuities (cracks on Fig. 7 (b)) and visible gradients, a single pair of measured displacement components is plotted in Fig. 7 for the zone Z1, and after the step 1 and step 2.

3. Results

A comparison between the conventional DIC and H-DIC is proposed to highlight the results obtained on simulated images. Three cases with a subset size of 64×64 pixels are proposed leading to evaluate the strain results and the location of cracks :

- Conventional approach: conventional DIC method coupled to finite difference method (DIC ε_{eqFD})
- Conventional enriched approach: HDIC method coupled to finite difference method (H-DIC ε_{eqFD})
- New proposed approach: H-DIC method using the first gradients of Eq. 1 (H-DIC $\varepsilon_{eq\frac{\partial U}{\partial X}}$)

Fig. 8 is plotted after the second loading/unloading cycle (ε_{p2}), which is more representative of the two mechanical behaviors (fracture and strain). It can be seen the same conclusion as for the mimicking images Fig. 2 (d)(f), retrieving the effects of the crack presence. Fig. 8 (a) shows that, using the FD method on conventional DIC measurements, large bands around the crack are significant and do not allow to discriminate the crack effect on the real strain values. Fig. 8 (b) shows H-DIC measurements using FD method where the strain errors are higher and do not allows to observe the zones of low strains. However, if the internal $\frac{\partial U}{\partial X}$ is used to calculate the equivalent strain H-DIC-$\varepsilon_{eq\frac{\partial U}{\partial X}}$ the crack effect is reduced and the real strains are less perturbed. This new proposed approach allows us to discriminate the precise crack localization and the strains.

Table 2 presents the average values of equivalent strain obtained using the three previous cases (DIC ε_{yFD}, H-DIC ε_{yFD} and H-DIC $\varepsilon_{y\frac{\partial U}{\partial X}}$) for the ten zones (Fig. 4). Values of strains correspond to average values calculated on the total area of each zones along the loading axis (y-axis). The errors are calculated using a global average (zone

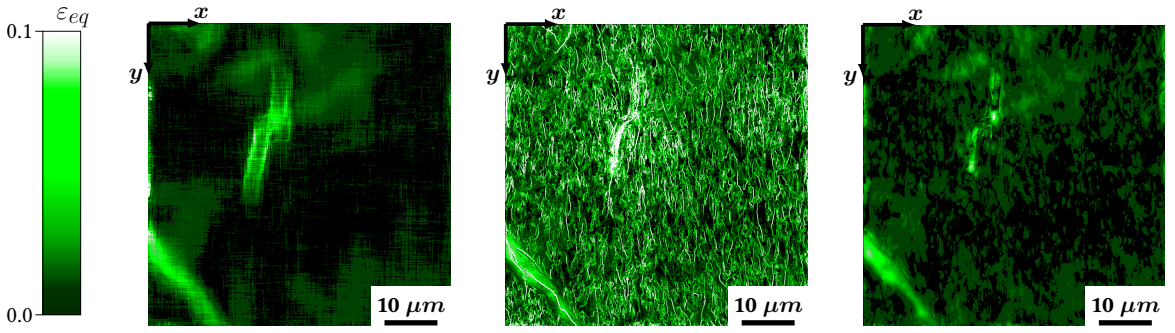

(a) DIC-ε_{eqFD} Step2 (b) HDIC-ε_{eqFD} Step2 (c) HDIC-$\varepsilon_{eq\frac{\partial U}{\partial X}}$ Step2

Figure 8: For Zone 10 Step2 and for subsets of 64×64 pixels equivalent strain computed from (a) DIC using FD method (ε_{eqFD}) , (b) H-DIC using FD method (ε_{eqFD}) and (c) H-DIC using first gradients ($\varepsilon_{eq\frac{\partial U}{\partial X}}$).

Table 2
Comparison between different mean compression strain values computed from, loading machine (Global ε_y), DIC ε_y, HDIC ε_{yFD} and H-DIC $\varepsilon_{ydU/dX}$ (+ defines 1-2 Pre-cracks on the zone and + + + defines large developed cracks on the zone). Measured mean values and standard deviations are presented for each studied zones

Mean Compression Strain								
%	Step 1 $\varepsilon_{p1} = 0.67\%$				Step 2 $\varepsilon_{p2} = 1.23\%$			
	DIC ε_y	H-DIC $\varepsilon_{y_{FD}}$	H-DIC $\varepsilon_{y\frac{\partial U}{\partial X}}$	Pre-Crack	DIC ε_y	H-DIC $\varepsilon_{y_{FD}}$	H-DIC $\varepsilon_{y\frac{\partial U}{\partial X}}$	Crack
Zone1	0.016 ± 0.182	0.005 ± 0.860	0.007 ± 0.182	+	1.100 ± 25.90	1.160 ± 26.20	1.080 ± 0.546	+++
Zone2	0.212 ± 0.210	0.220 ± 1.340	0.213 ± 0.219	-	0.903 ± 0.199	0.990 ± 1.430	0.904 ± 0.177	-
Zone3	0.380 ± 0.388	0.372 ± 3.460	0.374 ± 0.445	-	1.270 ± 0.599	1.240 ± 2.240	1.260 ± 0.570	-
Zone4	0.398 ± 0.256	0.400 ± 2.760	0.375 ± 0.249	+	1.496 ± 0.328	1.480 ± 3.200	1.380 ± 0.467	++
Zone5	0.218 ± 0.406	0.217 ± 1.160	0.222 ± 0.176	-	0.915 ± 0.551	0.919 ± 2.350	0.918 ± 0.283	-
Zone6	0.671 ± 0.163	0.670 ± 0.995	0.675 ± 0.182	-	1.670 ± 0.331	1.660 ± 1.840	1.580 ± 0.314	-
Zone7	0.099 ± 0.196	0.103 ± 1.570	0.110 ± 0.165	-	1.040 ± 0.240	1.050 ± 1.940	1.000 ± 0.230	+
Zone8	0.159 ± 0.145	0.166 ± 0.922	0.166 ± 0.156	+	0.846 ± 0.247	0.855 ± 1.270	0.840 ± 0.206	+
Zone9	0.205 ± 0.159	0.205 ± 1.270	0.206 ± 0.168	-	0.917 ± 0.203	0.924 ± 1.360	0.932 ± 0.170	-
Zone10	0.246 ± 0.183	0.277 ± 1.940	0.294 ± 0.202	+	0.590 ± 1.290	0.485 ± 9.550	0.571 ± 0.569	+++

dimension) of the local standard deviations (20×20 pixels). This principle is used to obtain an error evaluation only due to the noise level. For each step of loading, the measured values by DIC approaches is compared with the global value issued from the plate displacements of the loading machine. Moreover, one column for the step 1 describes if pre-cracks were observed on each zone and, for the step 2, crack column describes if developed cracks were detected. All observed pre-cracks and cracks were obtained using maps issued from H-DIC algorithm.

In Table 2 and for the two steps, it can be osberved that zones 3, 4 and 6 give higher mean strain values than the other zones. This can be attributed to an effect of the structure (3D), giving zones weaker than others.

After the first loading/unloading cycle, it can be noted that the reasidual compression strain values calculated from DIC and H-DIC are lower than ε_{p1} (except for zone 6). This fact can be directly linked to the earlier mentioned non-linear 'toe-in' portion of the stress-strain curve, relative to an in-homogeneous reparation of strains/stresses during the onset of the experiment. However, values of the strain calculated from the second step of loading are closer to ε_{p2} whatever the method used. A focus on the obtained standard deviations shows that for H-DIC ε_{yFD}, errors are 10 times higher than the other methods, retrieving the particular sensitivity to noise of this strain calculation method. Other method errors are near, but it can be noted that the presence of developed cracks (step 2, Z1 and Z10) induces a higher error level using classical strain evaluation with DIC. It can be also retrieved that, using H-DIC, it is necessary to employ the local first gradients to calculate the strain, compared to use the FD method. In what follows, only this last case H-DIC $\varepsilon_{y\frac{\partial U}{\partial X}}$ is used to analyze the local behavior of the sample.

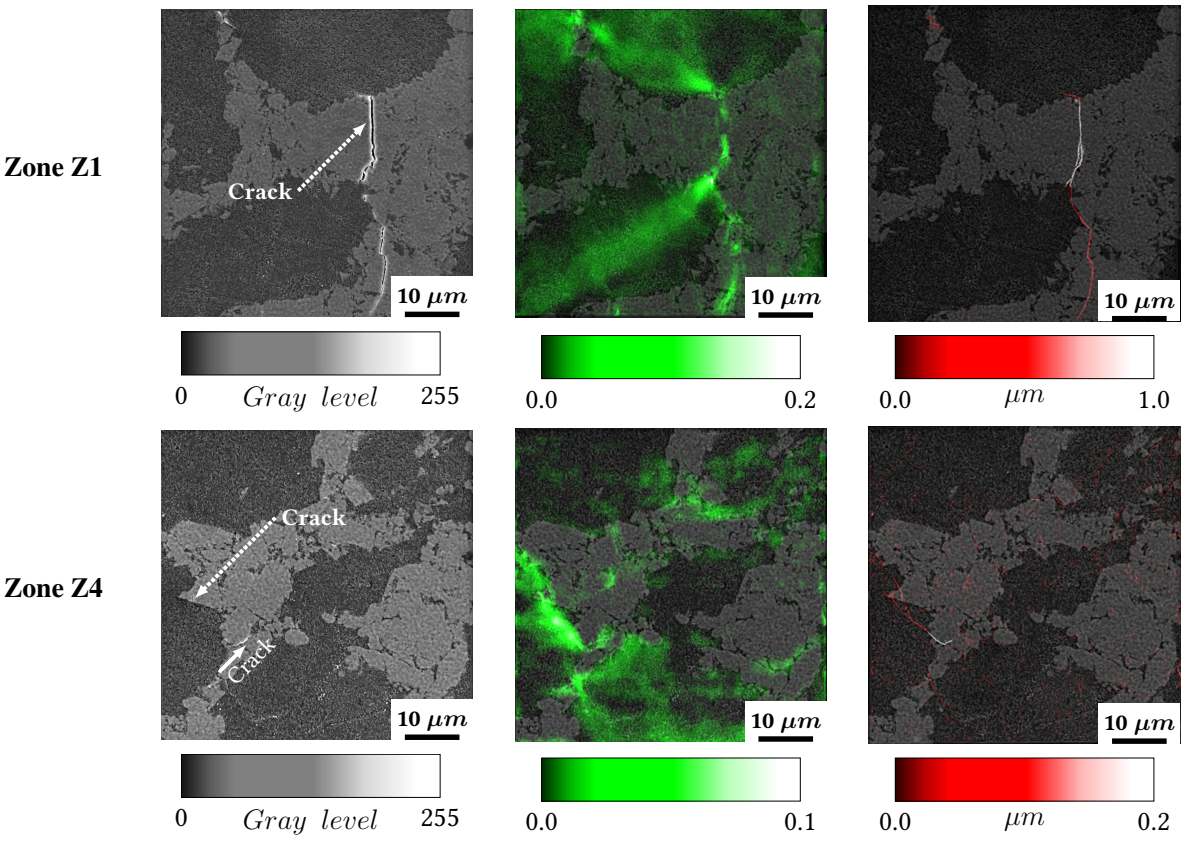

Figure 9: Maps after second loading/unloading cycle, and for tow zones (Z1, Z4). (a,d) SEM image, (b,e) equivalent strain H-DIC $\varepsilon_{eq\frac{\partial U}{\partial X}}$ and (c,f) norme of displacement jump vector $||\underline{U'}||$

4. Discussion

4.1. Focus on the second loading/unloading cycle

To highlight the efficiency of the new proposed approach, a focus of two zones is presented : Fig. 9 Z1 and Z4. These zones have the particularity, with coexisting cracks and residual strains. For each zone and after the second loading/unloading cycle, Fig. 9 presents the final SEM images, the equivalent strain maps extracted from the first gradients, and the jump maps $\underline{U'}$ (Eq. 1).

The strains and the cracks are well developed. It can be observed that the cracks are localized in the ω phase and near the interface of Al phase and ω phase, while the large strains are preferentially concentrated in the Al phase. This observation confirms that the ω phase has a brittle behavior while the Al phase has a ductile behavior. It can be noted that the local plasticity is developed from cracks, and can link, for example, two cracks. It can be interesting to see the initiation of these cracks using the first loading step, and observing micrographs to confirm their presences.

4.2. Focus on the first loading/unloading cycle

A focus on zones Z1 and Z4 are presented because they show the presence of pre-cracks (Fig. 10). The same observations and comments can be done with the zones Z8 and Z10. Fig. 10 (a) and (d) correspond to the pictures of the equivalent strain maps and the SEM images. It can be noted that the amplitude of strain ($0 < \varepsilon_{eq} < 0.05\%$) is lower than the strain error measured on simulated image (see Table 1). However, Fig. 10 (b) and (e) represent the superimposition between the $\underline{U'}$ map and the SEM image at the initial step, where it can be noted the presence of small cracks. Fig. 10 (c) and (f) are the micrographs and a zoom of red boxes from (b) and (e), where it can be observed the corresponding little cracks. Even if there is more noise in this step of loading, the cracks can be observed in the place where they were developed in the last step of loading. For example, the large crack in Fig. 9 (c) top left should be a

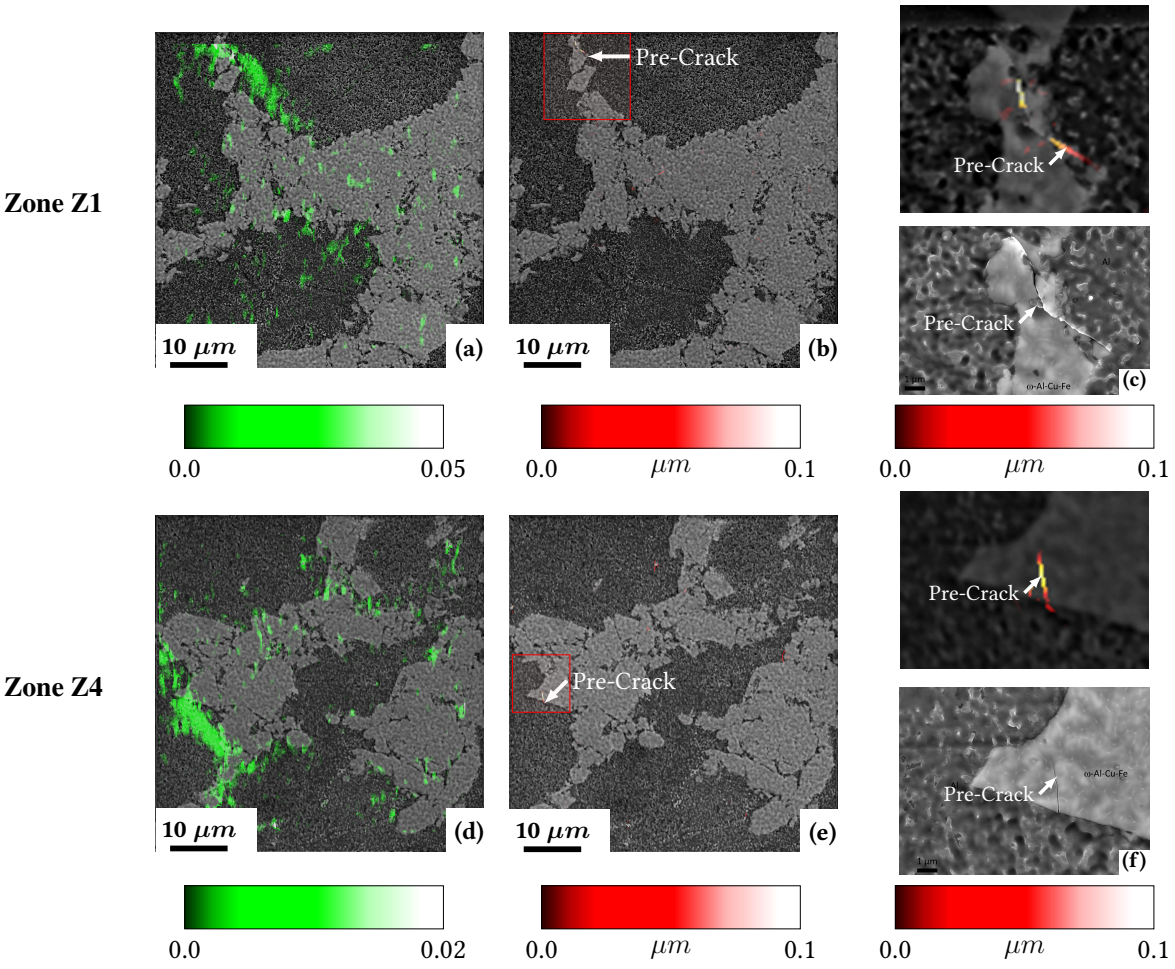

Figure 10: Crack initiation localization after the first loading/unloading cycle for two zones (Z1 and Z4). (a-d) Strain fields, (b-e) magnitude of displacement jump vector (red square), (c) and (f) zoom of the magnitude of displacement jump vector and SEM corresponding micrographies.

consequence of the propagation of the small crack observed in Fig. 10 (b). The same observation can be done with Fig. 10 (e) where the developed crack is initiated by the small one observed in Fig. 10 (d). It can be also seen that all observed pre-cracks are localized at an interface between Al and ω phases. This work confirms that, if it is necessary to measure strains in presence of pre-cracks and cracks during a mechanical process, H-DIC using $\frac{\partial U}{\partial X}$ offers a essential advantage.

5. Conclusions

The residual strain and fracture separation of a composite metallic material have been measured using experimental tools based on FIB-SEM-DIC. The H-DIC method were employed to solve the problem of kinematical discontinuities that result from plastic deformation and challenge conventional digital image correlation method DIC. Using this method, the strain directly calculated from a discontinuous displacement field generates a high level of strain errors. As it can be possible to extract the internal displacement jump (Eq. 1) to access to kinematical local movement (sliding and opening) and it is proposed to also use the first gradients to give access to local strain. This process gives the advantage to avoid a discontinuous field to access to strains (using FD method). To show the performances of this particular extraction, simulated images were created to mimic a crack surrounded by a strain field. The results have shown an excellent separation between the crack jump and the strain. It has been shown the advantage of using local

parameters instead of derivating discontinuous displacement fields.

The speckle patterns, which were necessary for the DIC methods, are created by milling using FIB, and finally SEM is used to capture images. To validate this process, histograms, auto-correlations and AFM profiles were used to evaluate the quality of the milling and imaging processes. The accuracy of the displacement linked to the stability of the SEM was evaluated to 0.05 pixel (6.25 nm), and give access to displacement jump of the crack, and the strains.

After this first validation and a short presentation of the analyzed material, the specimen was milled in ten zones distributed on the surface. Two loading/unloading cycles were applied to the specimen, using an ex-situ loading machine. Using the experimental images, the results obtained in the simulation part were retrieved, confirming better performances using local H-DIC parameters instead of derivated ones.

It has been shown that the FIB-SEM-DIC is a very suitable technique to study separately the cracks and the strains. It has been observed the two different behaviors of the two different phases of the tested material, highlighting the brittle behavior of the ω phase and the ductile behavior of the Al phase. A second analysis was done to focus on the initiation of some observed cracks. To do that, results were extracted after the first loading/unloading cycle and compared to micrographies of the sample surface. Two pre-cracks were observed at this state.

This experimental test demonstrates that the H-DIC method coupled with FIB milling and SEM Imaging is able to detect preliminary fractures, before their propagation. It also gives information about the microstructure response of a metallic composite material under strains. It gives the opportunity to better understand how strains and cracks are linked from each other, in a complex material under mechanical straining.

Acknowledgements

The authors gratefully acknowledge the support of LABEX Global. This work partially pertains to the French Government program "Investissements d'Avenir". (LABEX INTERACTIFS, reference ANR-11-LABX-0017-01).

This work has been partially supported by ≪ Nouvelle Aquitaine ≫ Region and by European Structural and Investment Funds (ERDF reference : P-2016-BAFE-94/95).

References

[1] Allais L, Bornert M, Bretheau T, Caldemaison D (1994) Experimental characterization of the local strain field in a heterogeneous elastoplastic material. Acta Metallurgica et Materialia 42(11):3865–3880, DOI 10.1016/0956-7151(94)90452-9

[2] Berfield TA, Patel JK, Shimmin RG, Braun PV, Lambros J, Sottos NR (2007) Micro- and nanoscale deformation measurement of surface and internal planes via digital image correlation. Experimental Mechanics 47(1):51–62, DOI 10.1007/s11340-006-0531-2

[3] Bertin M, Du C, Hoefnagels JPM, Hild F (2016) Crystal plasticity parameter identification with 3d measurements and integrated digital image correlation. Acta Materialia 116:321–331, DOI 10.1016/j.actamat.2016.06.039

[4] Besnard G, Guérard S, Roux S, Hild F (2011) A space–time approach in digital image correlation: Movie-DIC. Optics and Lasers in Engineering 49(1):71–81, DOI 10.1016/j.optlaseng.2010.08.012

[5] Bonneville J, Baluc N, Martin JL (1991) Deformation regimes in the intermetallic alloy, Ni_3Al. Proc. of int. symp. on intermetallic compounds, structure and mechanical properties, edited by O. Izumi. The Japan Institute of Metals pp 323–330

[6] Bourdin F, Stinville JC, Echlin MP, Callahan PG, Lenthe WC, Torbet CJ, Texier D, Bridier F, Cormier J, Villechaise P, Pollock TM, Valle V (2018) Measurements of plastic localization by heaviside-digital image correlation. Acta Materialia 157:307–325, DOI 10.1016/j.actamat.2018.07.013

[7] Chu TC, Ranson WF, Sutton MA (1985) Applications of digital-image-correlation techniques to experimental mechanics. Experimental Mechanics 25(3):232–244, DOI 10.1007/bf02325092

[8] Hedan S, Fauchille AL, Valle V, Cabrera J, Cosenza P (2014) One-year monitoring of desiccation cracks in tournemire argillite using digital image correlation. International Journal of Rock Mechanics and Mining Sciences 68:22–35, DOI 10.1016/j.ijrmms.2014.02.006

[9] Jin H, Bruck HA (2005) Pointwise digital image correlation using genetic algorithms. Experimental Techniques 29(1):36–39, DOI 10.1111/j.1747-1567.2005.tb00202.x

[10] Jin H, Lu WY, Haldar S, Bruck HA (2011) Microscale characterization of granular deformation near a crack tip. Journal of Materials Science 46(20):6596–6602, DOI 10.1007/s10853-011-5608-3

[11] Joseph A, Gauthier-Brunet V, Joulain A, Bonneville J, Dubois S, Monchoux JP, Pailloux F (2018) Mechanical properties of Al/ω- AlCuFe composites synthesized by the SPS technique. Materials Characterization 145:644–652, DOI 10.1016/j.matchar.2018.09.025

[12] Kammers AD, Daly S (2011) Small-scale patterning methods for digital image correlation under scanning electron microscopy. Measurement Science and Technology 22(12):125501, DOI 10.1088/0957-0233/22/12/125501

[13] Kammers AD, Daly S (2013) Digital image correlation under scanning electron microscopy: Methodology and validation. Experimental Mechanics 53(9):1743–1761, DOI 10.1007/s11340-013-9782-x

[14] Laplanche G, Joulain A, Bonneville J, Schaller R, Kabir TE (2010) Microstructures and mechanical properties of Al-base composite materials reinforced by AlCuFe particles. Journal of Alloys and Compounds 493(1-2):453–460, DOI 10.1016/j.jallcom.2009.12.124

[15] Li Y, Xie H, Luo Q, Gu C, Hu Z, Chen P, Zhang Q (2012) Fabrication technique of micro/nano-scale speckle patterns with focused ion beam. Science China Physics, Mechanics and Astronomy 55(6):1037–1044, DOI 10.1007/s11433-012-4751-4

[16] Li R, Zhu R, Chen S, He C, Li M, Zhang J, Gao P, Liao Z, Xu J (2019) Study of damage generation induced by focused helium ion beam in silicon. Journal of Vacuum Science & Technology B 37(3):031804, American Vacuum Society. DOI 10.1116/1.5096908

[17] Mansilla C, Ocelík V, and De Hosson J.T.M (2014) A New Methodology to Analyze Instabilities in SEM Imaging. Microscopy and Microanalysis. 1625–1637, volume 20. DOI 10.1017/s1431927614013282

[18] Mammadi Y, Joseph A, Joulain A, Bonneville J, Tromas C, Hedan S and Valle V (2019) Development of Optical Technique For Measuring Kinematic Fields in Presence of Cracks, FIB-SEM-DIC. Advancements in Optical Methods & Digital Image Correlation in Experimental Mechanics, Volume 3, Springer International Publishing 67–74, DOI 10.1007/978-3-030-30009-8_9

[19] Mello AW, Book TA, Nicolas A, Otto SE, Gilpin CJ, Sangid MD (2017) Distortion correction protocol for digital image correlation after scanning electron microscopy: Emphasis on long duration and ex-situ experiments. Experimental Mechanics 57(9):1395–1409, DOI 10.1007/s11340-017-0303-1

[20] Réthoré J, Hild F, Roux S (2007) Shear-band capturing using a multiscale extended digital image correlation technique. Computer Methods in Applied Mechanics and Engineering 196(49-52):5016–5030, DOI 10.1016/j.cma.2007.06.019

[21] Reu P (2014) All about speckles: Speckle size measurement. Experimental Techniques 38(6):1–2, DOI 10.1111/ext.12110

[22] Reu P (2015) All about speckles: Edge sharpness. Experimental Techniques 39(2):1–2, DOI 10.1111/ext.12139

[23] Reu P (2015) All about speckles: Speckle density. Experimental Techniques 39(3):1–2, DOI 10.1111/ext.12161

[24] Reyntjens S, Puers R (2001) A review of focused ion beam applications in microsystem technology. Journal of Micromechanics and Microengineering 11(4):287–300, DOI 10.1088/0960-1317/11/4/301

[25] Sabate N, Vogel D, Gollhardt A, Keller J, Cane C, Gracia I, Morante JR, Michel B (2007) Residual stress measurement on a MEMS structure with high-spatial resolution. Journal of Microelectromechanical Systems 16(2):365–372, DOI 10.1109/jmems.2006.879701

[26] Scrivens WA, Luo Y, Sutton MA, Collette SA, Myrick ML, Miney P, Colavita PE, Reynolds AP, Li X (2006) Development of patterns for digital image correlation measurements at reduced length scales. Experimental Mechanics 47(1):63–77, DOI 10.1007/s11340-006-5869-y

[27] Salvati E, Brandt L.R, Papadaki C, Zhang H, Mousavi S.M, Wermeille D, Korsunsky A.M (2018) Nanoscale structural damage due to focused ion beam milling of silicon with Ga ions. Materials Letters volume 213(2):346–349, DOI 10.1016/j.matlet.2017.11.043

[28] Stinville JC, Echlin MP, Texier D, Bridier F, Bocher P, Pollock TM (2015) Sub-grain scale digital image correlation by electron microscopy for polycrystalline materials during elastic and plastic deformation. Experimental Mechanics 56(2):197–216, DOI 10.1007/s11340-015-0083-4

[29] Sutton MA, Wolters WJ, Peters WH, Ranson WF, McNeill SR (1983) Determination of displacements using an improved digital correlation method. Image and Vision Computing 1(3):133–139, DOI 10.1016/0262-8856(83)90064-1

[30] Sutton MA, Mingqi C, Peters WH, Chao YJ, McNeill SR (1986) Application of an optimized digital correlation method to planar deformation analysis. Image and Vision Computing 4(3):143–150, DOI 10.1016/0262-8856(86)90057-0

[31] Sutton MA, Li N, Garcia D, Cornille N, Orteu JJ, McNeill SR, Schreier HW, Li X (2006) Metrology in a scanning electron microscope: theoretical developments and experimental validation. Measurement Science and Technology 17(10):2613–2622, DOI 10.1088/0957-0233/17/10/012

[32] Sutton MA, Schreier H, Orteu JJ (2009) Image Correlation for Shape, Motion and Deformation Measurements. Springer US, DOI 10.1007/978-0-387-78747-3

[33] Valle V, Hedan S, Cosenza P, Fauchille AL, Berdjane M (2014) Digital image correlation development for the study of materials including multiple crossing cracks. Experimental Mechanics 55(2):379–391, DOI 10.1007/s11340-014-9948-1

[34] Valle V, Bokam P, Germaneau A, Hedan S (2018) New development of digital volume correlation for the study of fractured materials. Experimental Mechanics DOI 10.1007/s11340-018-0415-2

[35] Valle V, Laou L, Léandry I, Yotte S, Rossignol S, Hedan S (2018) Crack analysis in mudbricks under compression using specific development of stereo-digital image correlation. Experimental Mechanics 58(3):475–486, DOI 10.1007/s11340-017-0363-2

[36] Zhu R, Xie H, Xue Y, Wang L, Li Y (2014) Residual stress measurement in thin films using a slitting method with geometric phase analysis under a dual beam (FIB/SEM) system. Measurement Science and Technology 25(9):095003, DOI 10.1088/0957-0233/25/9/095003

[37] Zhu R, Xie H, Xue Y, Wang L, Li Y (2015) Fabrication of speckle patterns by focused ion beam deposition and its application to micro-scale residual stress measurement. Measurement Science and Technology, DOI 10.1088/0957-0233/26/9/095601

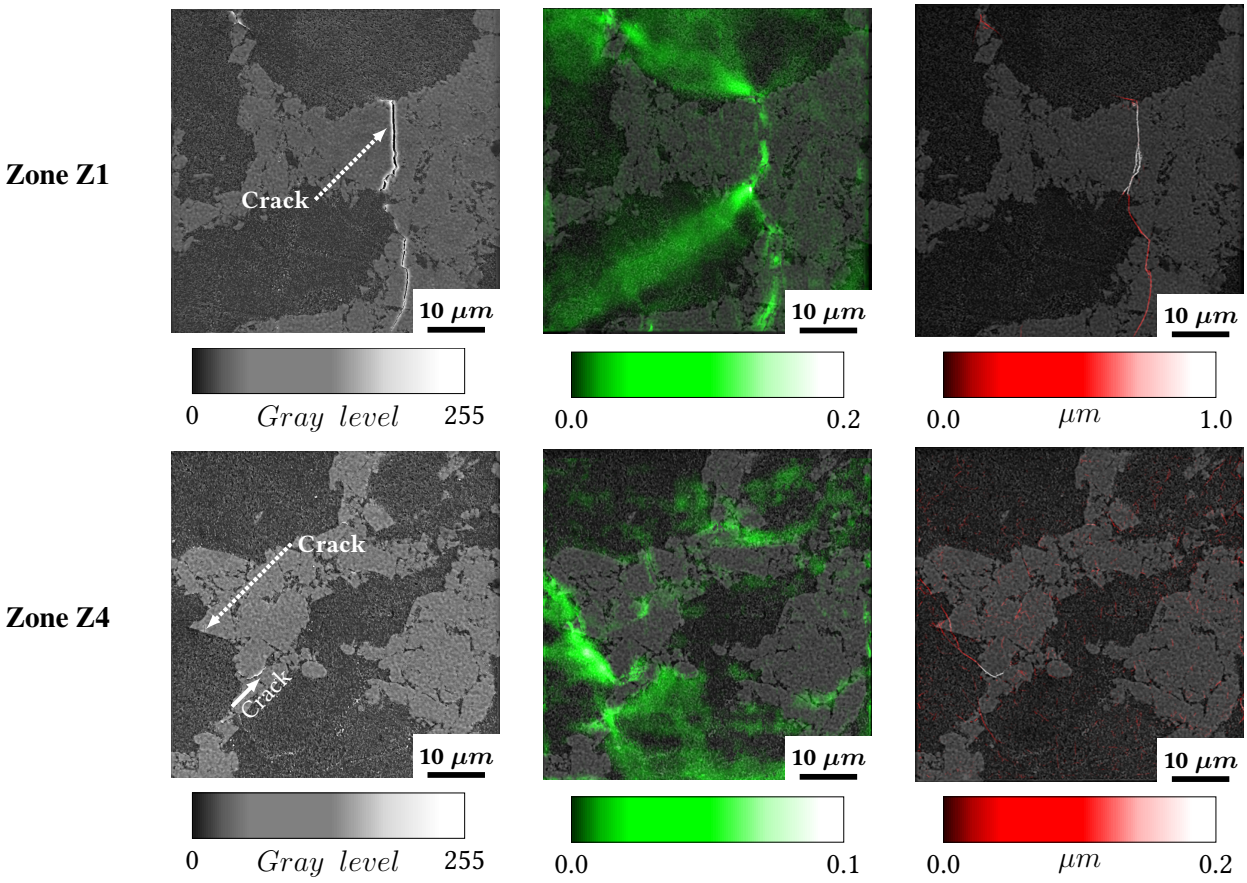

Compression test on a two-phase material Al/ω-Al-Cu-Fe, Maps after second loading/unloading cycle, and for tow zones (Z1, Z4). (a,d) SEM image, (b,e) equivalent strain H-DIC $\varepsilon_{eq\frac{\partial U}{\partial X}}$ and (c,f) norme of displacement jump vector $\|\underline{U'}\|$